

# Photonic Integrated Circuits for 5G-and-Beyond Networks: Enabling the mmWave Band and Beyond with InP-based Photomixers in Integrated Transceivers

Efstathios Andrianopoulos<sup>1, 6</sup>, Milan Deumer<sup>2</sup>, Tianwen Qian<sup>2</sup>, Nikolaos Lyras<sup>1, 6</sup>, Simon Nellen<sup>2</sup>, Evangelos Pikasis<sup>4</sup>, Georgia Ntouni<sup>4</sup>, Eleftherios Loghis<sup>4</sup>, Elias Tsirbas<sup>4</sup>, David de Felipe<sup>2</sup>, Panos Groumas<sup>5, 6</sup>, Christos Tsokos<sup>1, 6</sup>, Maria Massaouti<sup>1, 6</sup>, Christos Kouloumentas<sup>5, 6</sup>, Dimitrios Kritharidis<sup>4</sup>, Robert B. Kohlhaas<sup>2</sup>, Norbert Keil<sup>2</sup>, Martin Schell<sup>2,3</sup>, and Hercules Avramopoulos<sup>1, 6</sup>.

<sup>1</sup>Institute of Communication and Computer Systems, Athens, Greece

<sup>2</sup>Fraunhofer Heinrich Hertz Institute, Einsteinufer 37, 10587 Berlin, Germany

<sup>3</sup>Technical University Berlin, Institute of Solid State Physics, Hardenbergstraße 36, 10623 Berlin, Germany

<sup>4</sup>Intracom Telecom, 19.7 km Markopoulou Ave., Peania, Athens, Greece, 19002

<sup>5</sup>Optagon Photonics, Agia Paraskevi 15341, Athens, Greece

<sup>6</sup>School of Electrical and Computer Engineering, National Technical University of Athens, Athens, Greece

## ABSTRACT

Photonic integrated circuits (PICs) are one of the key enablers for beyond 5G networks. A novel generation of fully integrated photonic-enabled transceivers operating seamlessly in W- D- and THz-bands is developed within the EU funded project TERAway. Photonic integration technology enables key photonic functionalities on a single PIC including photonic up/down conversion. For efficient down-conversion at the photonic integrated receiver, we develop the first waveguide-fed photoconductive antenna for THz communications. Finally, we report on the experimental implementation of a fully photonic-enabled link operating across W- D- and THz-bands.

**Keywords:** Microwave Photonics, hybrid integration, photonic integration, photoconductive antennas, sub-THz communications, real-time communications, photonic integrated circuits

## 1. INTRODUCTION

The available spectral resources that reside within the W-, D- and THz-bands are considered as one of the key enablers for the future wireless communication systems. Wireless communication technology with carrier frequencies from 0.1 THz to 0.3 THz is designated as a promising candidate to fulfil the increasing demands for high data rates and large bandwidths in 5G and beyond wireless networks [1]-[3]. In this direction, towards the commercialization of wireless THz systems, significant effort has been given on the development of efficient solutions for the generation and detection of THz signals. Up to now, several approaches have been proposed and tested, employing both electronics-based as well as photonics-enabled solutions [4]. Although photonics-enabled solutions are generally less mature than their electronics-based counterparts, their inherent ability to cover seamlessly large parts of the THz electromagnetic spectrum renders them a promising solution for the exploitation of the available spectral resources in the THz regime, towards the beyond 5G era.

Photonics-enabled wireless THz communication links take advantage of photonic emitters based most commonly on PIN-PDs or UTC-PDs integrated with broadband antennas, and photonic receivers based on ultra-fast photoconductors suitable for down-conversion of the THz signal to an intermediate frequency (IF). Significant effort on the realization of such photonics-based wireless THz communication links have been performed, including hybrid solutions based on photonics-enabled emitters and electronic receivers [5], [6], as well as all-optical solutions employing photoconductive antennas (PCAs) at the receiver part of the link [7], [8].

Photonic integrated circuits (PICs) aim to be one of the key enablers for the networks beyond 5G (B5G). A novel generation of fully integrated photonics-enabled THz transceivers operating seamlessly in the W-, D-, and THz-bands is developed within the EU funded project TERAway [9]. Among others, novel InP active components including tunable lasers, modulators, photodiodes and PCAs are fabricated and integrated using a polymer-based photonic mainboard (PolyBoard) [10]. Photonic integration technology facilitates major photonic functionalities on a single PIC: optical frequency comb generation, injection locking, optical beam forming, and photonic up- and down-conversion to emit and receive wireless signals. A picture of the developed transmitter and receiver modules is depicted in Figure 1.

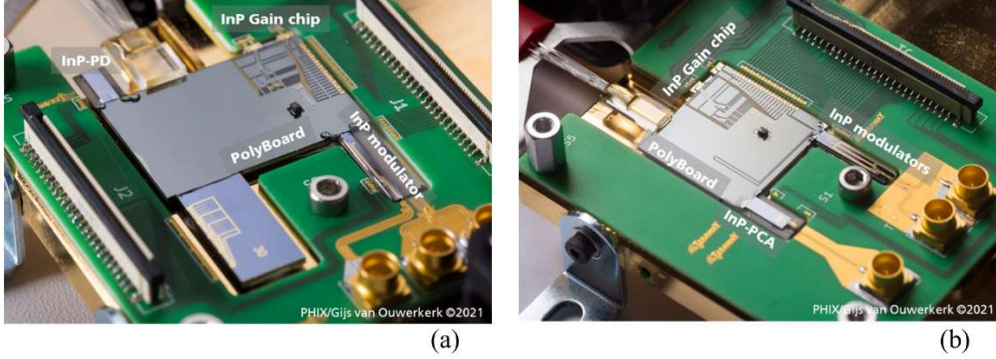


Figure 1. Hybrid photonic integrated circuits of the (a) transmitter and (b) receiver modules, integrating InP gain chips, modulators, photodiodes, and photoconductive antennas (PCAs) with the polymer-based photonic mainboard (PolyBoard), enabling up- and down-conversion of the THz signals.

This paper reports on some of the key achievements performed within the TERAway project [9]. Starting off, significant advancements on the design and fabrication of PCAs will be discussed, reporting on waveguide-fed PCA receivers as promising enablers of THz communications. Under that context, we will report on improvements on the design and fabrication of these PCAs, followed by a characterization of their performance. Moreover, we will report on the implementation of a TERAway-inspired all-optical real-time wireless link operating in the sub-THz regime. The real-time aspect of our testbed is enabled by a Baseband/Intermediate Frequency (BB/IF) unit responsible for the transmission and detection of QAM signals, implementation of the appropriate DSP methods, and extraction of key link quality assessment metrics in real-time such as the SNR, BER and the constellation diagrams. This link, being essentially a bulk implementation of TERAway's aspired concept, is based on all-optical components for the emission and detection of the wireless signal, implementing a PIN-PD-based emitter and a PCA-based receiver, both integrated with broadband antennas and packaged into fiber-pigtailed housing. The testbed's evaluation is performed in a homodyne scenario where a pair of lasers is equally split towards the transmitter and receiver path. A simulation analysis is briefly presented, followed by the corresponding experimental validation. Finally, the frequency response of our overall link is assessed, exhibiting error-free performance in frequency span from 90 to 310 GHz.

## 2. PHOTOCONDUCTIVE ANTENNAS ADVANCEMENTS

State-of-the-art PCAs, widely used for THz spectroscopy, are top-illuminated ultra-fast photoconductors. Photonic integrated circuits, however, rely on laterally illuminated waveguides to optically connect the active and passive components. So far, waveguide-coupled PCAs have only been demonstrated for pulsed THz emitters [11]-[13]. However, these devices are not suitable for integration in telecommunications PICs due to the vertical coupling via grating couplers. In addition, they are not compatible with 1550 nm technology and have limited responsivity.

Here, we report on a waveguide-fed PCA receiver, thereby realizing photonic integrated receivers for millimeter-wave and THz communication, for the first time. The benefit of the waveguide integration of the photonic THz detector is twofold. On one hand, it enables the integration of such devices in PICs as mentioned above. On the other hand, the responsivity of the receiver can be improved with waveguide coupling. In top-illuminated PCAs, the absorption of the incident light is limited by the thickness of the absorber [14]. Besides, carriers generated in the depth of the material do not contribute as much to the responsivity of the device as the carriers generated close to the contacts on the surface. Furthermore, in conventional PCAs the optical excitation has to pass through the interdigitated finger contacts on top of the photoconductor, which reduces the efficiency and increases the parasitic device capacitance. These drawbacks can be overcome by growing

the photoconductive element on top of a photonic waveguide through epitaxy. This way, the light from the waveguide can be coupled evanescently into the photoconductor. Consequently, the length of the photoconductive element can control the amount of light that gets absorbed rather than its thickness. Hence, all the photogenerated carriers are close to the electrical contacts as the thickness can remain small. Furthermore, the light does not have to pass the metal contacts in this configuration. Therefore, more light can be absorbed and the electrodes can be designed as two metal strips, which also simplifies the manufacturing process compared to interdigitated finger structures.

Note that the optical power available at the input of each component of a PIC is low. Typically, only a few milliwatts can be expected, whereas fiber-coupled PCAs are operated with several tens of milliwatts of optical power using Erbium-Doped Fiber Amplifiers (EDFA)s [14]. Therefore, the responsivity of the PCA used in PICs must be increased further. This can be achieved by taking advantage of the waveguide coupling and monolithically integrating the receiver with a semiconductor optical amplifier (SOA).

For this work, we designed waveguide-integrated photoconductors based on indium gallium arsenide (InGaAs) using the simulation tools FIMMWAVE and HFSS. We then manufactured such devices together with SOAs on a single wafer employing multiple epitaxy overgrowths as well as photolithography steps. Figure 2 (b) shows a micrograph of a receiver chip with waveguides, SOA and PCA. We characterized the device in a homodyne spectroscopy setup to compare them to state-of-the-art top-illuminated PCAs [14]. The results are shown in Figure 2 (a). Here, the normalized detected power is depicted over the operating frequency. We normalized the power to the value measured with the conventional PCA driven with 15 dBm of optical power at 322 GHz, i.e. the highest target frequency for THz communication in the W-, D-, and THz-band. It can be seen that our novel device has approximately 4 dB higher detector power at 322 GHz while it is only operated at 0 dBm optical power. In addition, the frequency response of the new photonic integrated PCA is flat compared to the state-of-the-art. Between the lower and upper edge of the target range (92 – 322 GHz), the detected signal decreases by 5 dB only, which is mainly attributed to the decreasing emitted power of the THz transmitter in the testbed [15]. Thus, we successfully designed and demonstrated a waveguide-integrated PCA and monolithically integrated it with an SOA to create a photonic THz receiver that can be employed in photonic THz communication PICs.

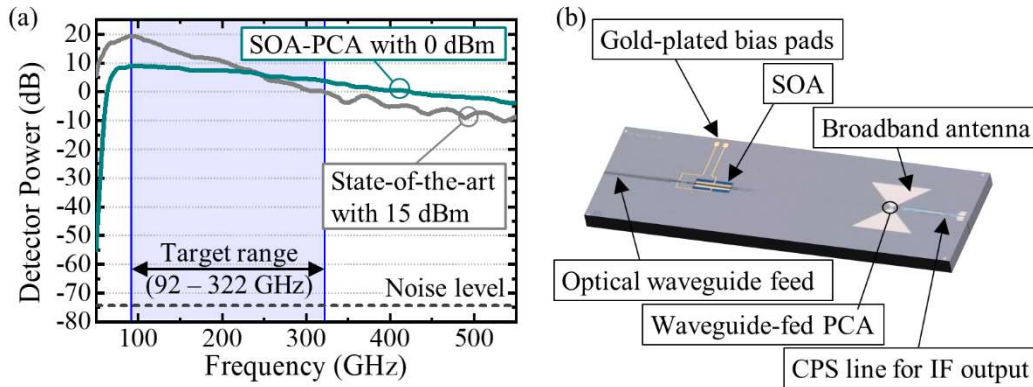


Figure 2. (a) Frequency response of a state-of-the-art PCA receiver with 15 dBm optical input and an SOA-integrated PCA with 0 dBm optical feed. The detected power is normalized to the highest frequency of our target range (322 GHz). (b) A micrograph of the SOA-integrated PCA chip with coplanar strip-line as electrical output that allows for intermediate frequencies up to several GHz.

### 3. BASEBAND AND INTERMEDIATE FREQUENCY UNIT

The design of the higher carrier frequencies communication systems is mainly a twofold issue, on one side the choice of efficient modulation schemes, and on the other side the low complexity of the development of an efficient sub-THz system.[16], [17]. Higher carrier frequency systems above the E-band (e.g. in the D-band or the sub-THz band) occupy larger bandwidth channels, so the usage of suitable and low-complexity modulation schemes is crucial.

Multi-Carrier (MC) modulations are a possible solution for future sub-THz communication systems as they have been widely used in many wireless systems [16]. But the MC sub-THz communication systems inherit the major issues of the

multi-carrier modulations such as high peak-to-average ratio (PAPR), strict synchronization and high sensitivity to Doppler effects. Also, due to limited multipath components in these high frequencies, the channel exhibits a frequency-flat selectivity [16]. Recently, a comparative study of MC and Single Carrier (SC) modulation schemes for THz communications was published presenting their features in terms of complexity and performance, taking into account the peculiarities of the indoor/outdoor THz channel for different scenarios [18].

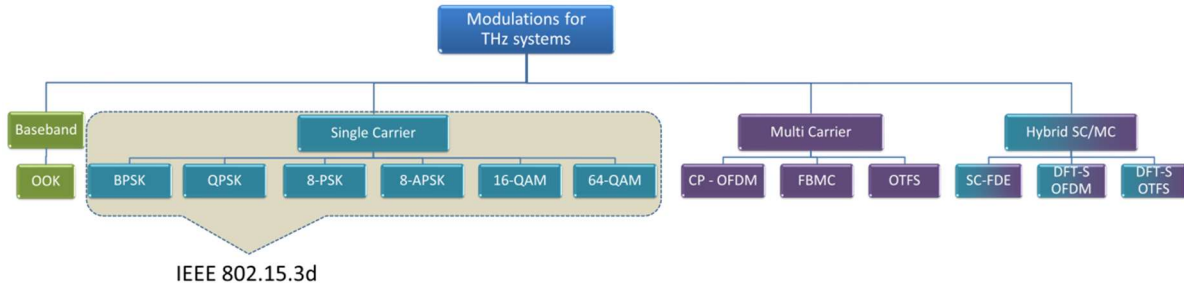


Figure 3. Proposed candidate modulation schemes for future THz communication systems

On the flip side, SC schemes for these higher frequencies are proposed as spectral and energy-efficient candidate solutions for sub-THz wireless communications offering the prospect of large signal bandwidths [16][18]. The IEEE 802.15.3d, as the first worldwide standard, was released in 2018 for wireless communications in the sub-THz frequency band from 252 GHz to 321 GHz [19]. The standard suggests 8 different channel bandwidths from 2.16 GHz to 69.12 GHz in multiples of 2.16 GHz. Two PHY-modes (THz-SC PHY and THz-OOK PHY) with 7 simple modulation schemes like on-off keying (OOK), binary and quadrature phase shift keying (BPSK, QPSK,  $\pi/2$ -BPSK,  $\pi/2$ -QPSK), and higher modulation formats like 16-quadrature amplitude modulation (QAM) and 64-QAM are proposed by this standard [19]. Figure 3 shows some of the proposed modulation schemes for future THz communication schemes, dividing them into baseband, SC, MC, and hybrid SC/MC.

For the needs of the TERAway project, an appropriate baseband unit was selected based on Intracom Telecom's E-band product line, enabling the operation of a channel with a symbol rate up to 1.6 GBaud and modulation formats up to SC 256-QAM [20]. All the demanding digital signal processing (DSP) required for the baseband transmission and reception, was performed on a FPGA-based board.

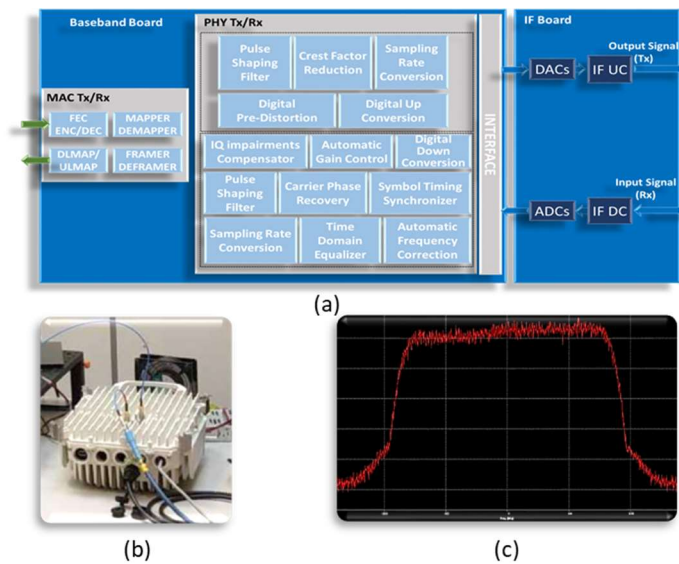


Figure 4. (a) A conceptual block diagram of the BB/IF unit (b) the enclosed integrated BB/IF unit that was used in this experimental setup, and (c) the magnitude power spectrum of the baseband QAM signals was produced by the baseband unit

On the transmitter side, the DSP methods perform the encapsulation of Ethernet packets inside wireless transmission frames and the coding of these frames using Forward Error Correction (FEC) codes and formats up to 256-QAM. Moreover, the DSP implementation includes processes such as filtering for sampling rate conversion, pulse shaping and the DAC interface. On the receiver side, the baseband processor performs signal decoding using clock recovery, equalization, sub-THz specific impairments' cancellation, phase and symbol recovery, FEC decoding and the final extraction of the Ethernet packets. A printed circuit board (PCB) for the Intermediate Frequency Unit (IFU) has been developed specifically for this project. This PCB includes the DA/AD converters to generate/acquire the in-phase and quadrature (I/Q) data streams as well as the required I/Q modulators/demodulators for the up/down conversion processes. Figure 4(a) displays an abstract block diagram of the real-time BB/IF unit, while Figure 4(b) shows the unit enclosed in its metallic cover for cooling and shielding purposes. The magnitude power spectrum of the generated QAM signals by the BB unit is depicted in Figure 4(c).

#### 4. EXPERIMENT SETUP & MEASUREMENTS RESULTS

In addition to the device development and module assembly, we will report on the first fully photonic-enabled real-time link operating across the W-, D-, and THz-bands, enabled by the devices discussed in the previous sections of the present manuscript. The testbed is enabled by a PIN-PD-based emitter [6], [15] and a receiver based on an ultra-fast photoconductor [21]. Both optical devices have integrated broadband antennas mounted on a silicon lens enabling free-space radiation and detection of wireless sub-THz signals, and are packaged into a fiber-pigtailed housing. The real-time generation and detection of the information signal is performed by the aforementioned BB/IF unit, that transmits QPSK signals at a fixed symbol rate of 1.6 GBaud, accounting for a total bit rate of 3.2 Gb/s. Our setup was tested in a homodyne scenario using the same pair of lasers at the transmitter and receiver side for the generation and detection of the wireless signals. Moreover, a theoretical analysis of the expected performance of our testbed focusing on key microwave photonics analog metrics, allowed us to optimize the performance of our link, cross-validating the simulation outcomes with the experimental results.

Figure 5 depicts a schematic representation of the experimental setup. Two tunable laser sources (TL 1 and TL 2) are split equally by two 3-dB splitters, towards the transmitter (Tx) and receiver (Rx) part of our testbed. The two laser sources are spaced frequency-wise by  $f_{\text{THz}}$ , which corresponds to the targeted sub-THz frequency of our link. At the transmitter part, the first tunable laser is modulated by means of a Mach-Zehnder Modulator (MZM) at an intermediate frequency (IF)  $f_{\text{IF}}=5$  GHz by a QPSK signal of 1.6 GBaud symbol rate, generated by the BB/IF unit. As a result of this modulation process, two optical sidebands are generated at a distance equal to the IF, around the optical carrier which is placed at  $f_0$ . The output of the MZM is forwarded to an EDFA where it is amplified, and then to an optical bandpass filter (OBPF) operating in a single sideband suppressed carrier (SSB-SC) scheme, responsible for filtering out the optical carrier and one of the two optical sidebands. The two paths at the Tx are then amplified by EDFAs and are coupled together using a 3-dB optical coupler in order to be forwarded to the photonic emitter. A variable optical attenuator (VOA) has been implemented allowing us to assess at each time the optical power that is inserted to the emitter, and a 1% tap splitter acts as a monitoring interface of the emitter's optical input. The PIN-PD-based emitter will then down-convert the optical signal to the sub-THz domain and radiate it at a frequency defined by the difference of the frequencies of the two optical spectral components equal to  $f_{\text{rad}} = f_{\text{THz}} + \text{IF}$ , since the upper optical sideband was filtered out during the filtering process. Off-axis parabolic mirrors with 2-inch diameter and 3-inch focal length are placed both after the output of the Tx and before the input of the Rx to increase the antenna gain and guide the transmitted beam across 1 m of free-space with ambient air.

At the receiver part, the two optical sources are coupled together and are amplified by means of an EDFA. The two-tone optical signal is then forwarded to the photonic THz receiver, where the PCA generates a photonic local oscillator (PLO) using the beat signal of the two optical tones, and down-converts the signal by a frequency equal to the frequency difference of the two tones, i.e.,  $f_{\text{THz}}$ . As a result of this process, the signal at the output of the photonic PCA-based receiver is placed at a frequency equal to the IF, i.e. the offset frequency generated by the BB/IF unit. The IF signal is then forwarded to an analog microwave chain comprising a pair of low-noise amplifiers (LNAs) and an electrical bandpass filter (BPF), before serving as an input to the BB/IF unit's Rx port. The BB/IF unit will then receive the IF signal and perform the I/Q down-conversion, where the produced distorted QAM signals are captured by the ADCs. During the baseband processing, the I/Q data streams are recovered, and DSP functions are applied in real-time including symbol timing, frame synchronization, carrier frequency offset cancelation, phase noise correction, filtering, equalization, RF impairments compensation, symbol



de-mapping, and FEC decoding. Finally, the BB/IF unit extracts key performance indicators such as the constellation diagram, the signal-to-noise ratio (SNR) and the bit-error ratio (BER) in real time, allowing us to assess at each moment the quality of our link. The BER is calculated by comparing the bit sequence transmitted to the one received at each time frame, thus providing real BER measurements. On the other hand, the SNR is estimated by the extracted constellation diagram after DSP has been applied.

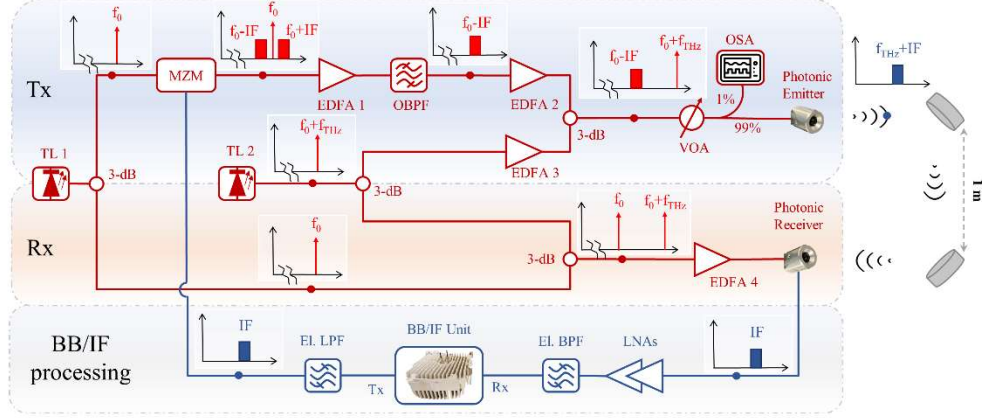


Figure 5: Schematic representation of the experimental setup

A theoretical analysis followed by the appropriate simulation tools on key analog optical link (AOL) metrics has been performed allowing us to assess and optimize the quality of our link. The analysis focused on the transmitter part of the setup, and more specifically on the proportion of the optical power of each patch comprising the Tx, i.e., the path carrying the optical sideband placed at  $f_0 - IF$  and the path carrying the optical carrier generated by TL 2, placed at  $f_0 + f_{THz}$ . By performing a standard single tone analysis [22], we calculated the theoretical optical field at each point of the optical chain, leading to the following expression for the generated photocurrent at the photodetection stage:

$$I_{DC} = \frac{1}{4} \cdot r_{PD} \cdot \left[ \frac{g_{EDFA1} \cdot g_{EDFA} \cdot P_o \cdot J_1(\hat{\varphi})^2}{4 \cdot l_{SB}} + \frac{P_o \cdot g_{EDFA}}{l_{CW}} \right] \quad (1)$$

In Equation (1),  $r_{PD}$  is the responsivity of the PIN-PD,  $g_{EDFAi}$  is the gain factor of the  $i$ -indexed EDFA depicted in Figure 5,  $P_o$  is the optical power of the tunable lasers,  $l_{SB}$  and  $l_{CW}$  correspond to the overall optical losses that the modulated path and the unmodulated path respectively meet until the photodetection, and  $J_1(\hat{\varphi})$  represents the 1<sup>st</sup> order Bessel function of the first kind, having as index the term:  $\hat{\varphi} = \frac{\pi \hat{V}_m}{V_\pi}$ . Here,  $\hat{V}_m$  is the amplitude of the transmitted signal generated from the BB/IF unit, and  $V_\pi$  is the halfwave voltage of the MZM. Equation (1) can be separated into two terms, with the first term corresponding to the contribution of the modulated path to the overall DC photocurrent, and the second term corresponding to the respective contribution of the unmodulated path.

A key metric that defines the performance of an AOL is the noise factor [22], which can be described as the quotient of the SNR at the input of the AOL to the SNR at its output, thus straight-forwardly assessing the quality degradation of the link. The noise factor is commonly expressed in decibels as the noise figure, as:

$$NF [dB] \equiv N_{out}[dBm/Hz] - 10\log_{10}(k_B T_s) - G[dB], \quad (2)$$

where  $N_{out}$  is the total noise power spectral density after the photodetection stage,  $k_B$  is Boltzmann's constant,  $T_s$  is the standard noise temperature equal to 290 K, and  $G$  is the link's gain factor.

By applying the aforementioned analysis into our demonstration scenario, we calculated the noise figure as a function of the ratio of the DC photocurrent generated by the modulated path of the transmitter to the total DC photocurrent generated at the PIN-PD. Figure 6 depicts the corresponding results. As can be observed from the figure, the simulation results suggested that better link performance could be achieved by having a smaller proportion on the modulated path (denoted

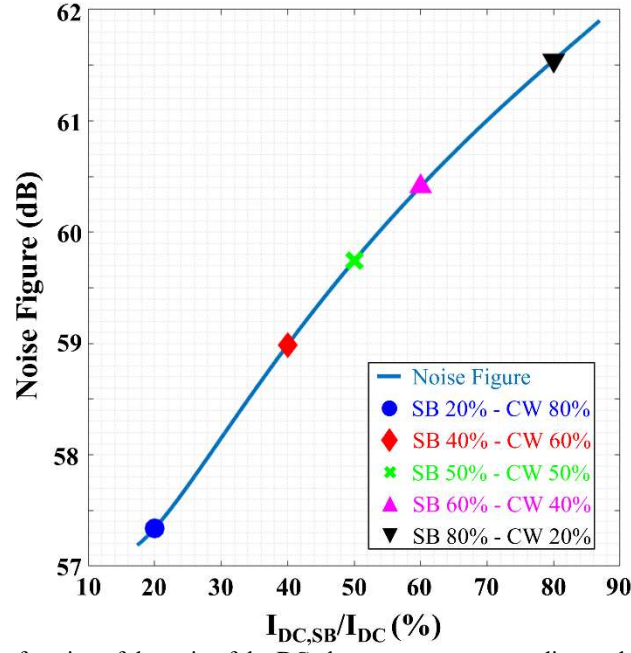


Figure 6. Simulated Noise Figure as a function of the ratio of the DC photocurrent corresponding to the unmodulated path, to the total generated DC photocurrent.

as SB in the figure) and therefore a higher proportion in the unmodulated path consisting only of the continuous wave tone generated by TL 2 (depicted as CW in the figure). The proportions of the two DC photocurrent terms were configured by adjusting the gains of EDFAs 2 and 3 which correspond to the two paths separately. This imbalance can be understood considering the successive amplification stages of the modulated sideband path. More specifically, higher gain values of EDFA 2 cause a significant increase in the amplified spontaneous emission (ASE) noise of EDFA 1, which remains in-band to the information signal's spectral content after photodetection, thus rendering this noise source the limiting noise source of our system. Respectively, lower gain values of EDFA 2 alleviate this issue, and by increasing the gain of EDFA 3 the power of the emitted sub-THz signal remains the same, defined by the multiplication of the two optical spectral

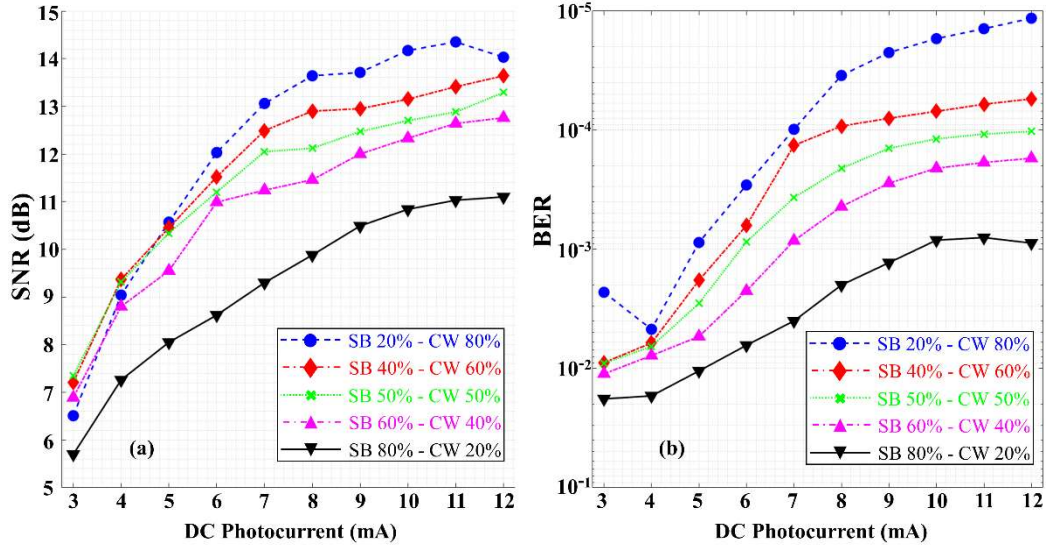


Figure 7. Real-time measurements of the (a) SNR and (b) BER values, as a function of the DC photocurrent generated at the emitter, for different proportion percentages of the DC photocurrent generated at each path of the Tx.

components before photodetection. In the figure, five different proportion settings are marked in the noise figure curve, corresponding to the proportions tested during the experimental campaigns.

Figure 7 (a) and (b) depict the SNR and BER values respectively, as they were extracted in real time through the BB/IF unit, with respect to the generated DC photocurrent. We note at this point that the generated photocurrent is directly proportional to the emitted THz power [6]. The central frequency of the sub-THz signal was set at 110 GHz. In each figure, different curves described in the legend of the figure, correspond to the different proportions of the DC photocurrent generated by each path, with the total DC photocurrent in all cases adding up to the respective x-axis value of the figure. The proportions of each path were set by adjusting the pump current of the EDFA, always within its linear operating range. The photocurrent was swept by carefully adjusting the VOA before the emitter's input. As observed, the experimental studies exhibit the trend that was suggested from the simulation studies, with better performances being observed when the DC photocurrent generated by the unmodulated path dominates the total generated DC photocurrent. The best performance was observed when the proportions of the sideband to the CW path were equal to 1:4, where a best case pre-FEC BER of  $1.16 \cdot 10^{-5}$  was achieved for a photocurrent value of 12 mA. Overall, the link showed robust performance even for small values of the photocurrent, showing error-free performance post-FEC encoding in all cases presented.

Finally, we assessed the frequency response of our link. The tuning of the central frequency was performed by keeping the optical carrier of the modulated path (TL 1) fixed, while tuning the carrier of the unmodulated path (TL 2). Figure 8 depicts the frequency-relative measurements of the real-time SNR and BER, as they were acquired from the BB/IF unit. The central frequency of the THz signal spans from 90 GHz up to 310 GHz, with a frequency interval of 20 GHz between each measurement. As can be observed, frequencies below 100 GHz exhibit higher losses, since the modules were originally designed for operation beyond the 100 GHz mark. The link exhibits a peak at 110 GHz, and as the frequency increases, the SNR steadily decreases. However, even at the 310 GHz case the obtained pre-FEC BER is equal to  $3.9 \cdot 10^{-2}$ , which is within the BB/IF units correction capabilities with the appropriate FEC encoding. Therefore, our link showcased an error-free performance at a 220 GHz span (90-310 GHz), fully aligning with TERAway's ultra-broadband vision.

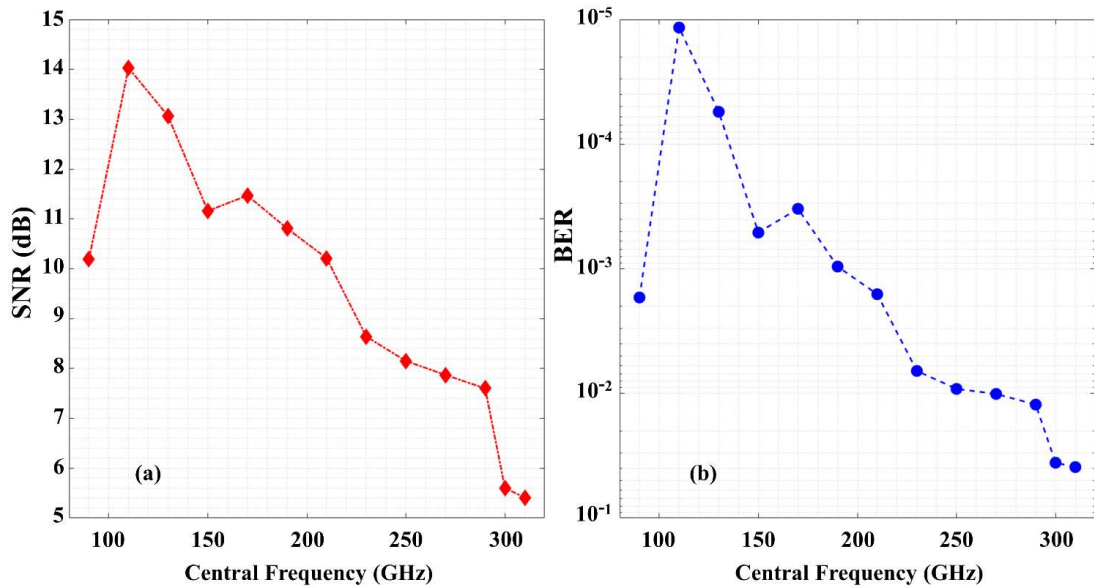


Figure 8. Real-time measurements of the (a) SNR and (b) BER values, as a function of the central frequency of the signal

## 5. CONCLUSIONS

In this work, some of the main advancements achieved within the EU funded TERAway project are presented. Firstly, leveraging multi-platform photonic integration, a novel fully integrated photonics enabled transceiver is presented. The transceiver hosts multiple optical functionalities, including among others InP-based photodiodes and PCAs responsible for the up- and down-conversion of the THz signals. Moreover, the paper reports on the development of a novel waveguide-



fed PCA receiver. Due to on-chip optical amplifiers, our receiver requires 15 dB less optical input for operation than state-of-the-art PCAs. Within the target frequency range of TERAway project (92-322 GHz) our PCA exhibited a very flat frequency response rendering our receiver a very promising solution enabling all-optical millimeter-wave and THz communications. In addition to the device development and module assembly, we also demonstrated a real-time wireless link operating across the W-, D- and THz-bands. The real-time generation and detection of the information signal was performed by an appropriate BB/IF unit, operating with 1.6 GBaud QPSK signals, for a total of 3.2 Gb/s throughput. Among others, the BB/IF unit performs real-time DSP methods both at the transmitted and the received signal, and allows us to assess the performance of our link in real-time, extracting key metrics such as the BER, the SNR and the constellation diagram. A brief theoretical analysis has been presented on the expected performance of the link, followed by an experimental validation of the simulation outcomes. Finally, the broadband aspect of our link was validated, with an error-free real-time performance being observed in frequencies spanning from 90-310 GHz.

## ACKNOWLEDGEMENTS

The work was supported by the EU-funded project ICT-TERAway (GA No. 871668).

## REFERENCES

- [1] H.-J. Song and T. Nagatsuma.: ‘Present and future of terahertz communications’, *Trans. THz Sci. Technol.*, 2011, 1, (1), pp. 256–263
- [2] Y. Niu, Y. Li, D. Jin, L. Su, and A. V. Vasilakos, “A survey of millimeter wave communications (mmWave) for 5G: opportunities and challenges,” *Wirel. Netw.*, vol. 21, pp. 2657–2676, 2015.
- [3] S. Rommel, T. R. Raddo, and I. Tafur Monroy, “Data center connectivity by 6G wireless systems,” in *Proc. Photon. Switching Comput.*, Sep. 2018, pp. 1–3.
- [4] T. Nagatsuma, G. Ducournau, and C. C. Renaud, "Advances in terahertz communications accelerated by photonics," *Nat. Photon.*, vol. 10, no. 6, pp. 371-379, Jun. 2016
- [5] H.-J. Song, et al., “24 Gbit/s data transmission in 300 GHz band for future terahertz communications” *Electronics Letters*, 2012, 48, (15), p. 953-954, DOI: 10.1049/el.2012.1708IET Digital Library
- [6] S. Nellen et al., "Coherent Wireless Link at 300 GHz With 160 Gbit/s Enabled by a Photonic Transmitter," in *Journal of Lightwave Technology*, vol. 40, no. 13, pp. 4178-4185, 1 July1, 2022, doi: 10.1109/JLT.2022.3160096.
- [7] T. Harter et al., "Wireless THz link with optoelectronic transmitter and receiver," *Optica* 6, 1063-1070(2019
- [8] A Morales et al., "Highly Tunable Heterodyne Sub-THz Wireless Link Entirely Based on Optoelectronics," in *IEEE Transactions on Terahertz Science and Technology*, vol. 11, no.3, pp. 261-268, 2021, doi:10.1109/TTHZ.2021.3064188
- [9] <https://ict-teraway.eu/>
- [10] T. Qian, et al., (2022, March). ‘Hybrid Polymer THz Receiver PIC with Waveguide Integrated Photoconductive Antenna: Concept and 1st Characterization Results’. In *Optical Fiber Communication Conference* (pp. W3D-6). Optica Publishing Group.
- [11] S. Al-Daffaie, et al., “Terahertz nanodevices for photonic integrated circuits,” 1200503(March), 3 (2022).
- [12] P. Chen, M. Hosseini, and A. Babakhani, “An integrated germanium-based THz impulse radiator with an optical waveguide coupled photoconductive switch in silicon,” *Micromachines*, vol. 10, no. 6, pp. 1–10, 2019, doi: 10.3390/mi10060367
- [13] H. Page, et al., “Waveguide coupled terahertz photoconductive antennas: Toward integrated photonic terahertz devices,” *Appl. Phys. Lett.*, vol. 92, no. 16, 2008, doi: 10.1063/1.2909539.
- [14] M. Deumer, et al., "Continuous wave terahertz receivers with 4.5 THz bandwidth and 112 dB dynamic range," *Opt. Express* 29(25), 41819 (2021).

- [15] S. Nellen, et al., "Radiation pattern of planar optoelectronic antennas for broadband continuous-wave terahertz emission," *Opt. Express* 29(6), 8244–8257 (2021).
- [16] H. Sarieddeen, M.-S. Alouini and T. Y. Al-Naffouri, "An overview of signal processing techniques for terahertz communications", *Proc. IEEE*, vol. 109, no. 10, pp. 1628-1665, Oct. 2021.
- [17] M. S. D. Shehata, et al., "IEEE 802.15.3d-compliant waveforms for terahertz wireless communications", *J. Lightw. Technol.*, vol. 39, no. 24, pp. 7748-7760, Dec. 2021.
- [18] S. Tarboush, H. Sarieddeen, M.-S. Alouini and T. Y. Al-Naffouri, "Single-versus multi-carrier terahertz-band communications: A comparative study" in *arXiv:2111.07398*, 2021.
- [19] IEEE, 802.15.3d-2017, "IEEE Standard for High Data Rate Wireless Multi-Media Networks–Amendment 2: 100 Gb/s Wireless Switched Point-to-Point Physical Layer", Oct. 2017.
- [20] [http://www.intracom-telecom.com/downloads/pdf/products/wireless\\_access/Ultralink.pdf](http://www.intracom-telecom.com/downloads/pdf/products/wireless_access/Ultralink.pdf)
- [21] S. Nellen et al., "Fiber-coupled, photoconductive receiver for heterodyne detection up to 1 THz stabilized by an optical frequency comb," 2017 42nd IRMMW-THz
- [22] J. Urick, Keith J. Williams, Jason D. McKinney, *Fundamental of microwave photonics*. Hoboken, NJ, USA: John Wiley & Sons, 2015, pp.273-311.